Ligand discrimination in hOR1A1 based on the capacitive response

Anna Lagunas, Christine Belloir, Maxence Lalis, Loïc Briand, Jérémie Topin, Pau Gorostiza, Josep Samitier

Ligand discrimination in hOR1A1 based on the capacitive response

Anna Lagunas[1,2,*], Christine Belloir[3], Maxence Lalis[4], Loïc Briand[3], Jérémie Topin[4], Pau Gorostiza[2,5,1], Josep Samitier[2,6,1]

[1]CIBER-BBN, ISCIII, Madrid, Spain

[2]Institute for Bioengineering of Catalonia (IBEC), Barcelona Institute of Science and Technology, Barcelona, Spain

[3]Centre des Sciences du Goût et de l'Alimentation, CNRS, INRAE, Institut Agro, Université de Bourgogne, F-21000 Dijon, France

[4]Institut de Chimie de Nice, Université Côte d'Azur, Nice, France

[5]Catalan Institution for Research and Advanced Studies (ICREA), Barcelona, Spain

[6]Department of Electronics and Biomedical Engineering, Faculty of Physics, University of Barcelona (UB), Barcelona, Spain

*Corresponding author: Anna Lagunas alagunas@ibecbarcelona.eu

Abstract

The mechanisms of odor discrimination are based on the differential interactions of odorant molecules with olfactory receptors (ORs). The biohybrid sensors described so far using ORs show selectivity towards specific versus non-specific binding. Here we disclose a method that enables odorant discrimination based on modulation of the capacitive response of the receptor that allows differentiation of three high-affinity hOR1A1 agonists. We performed voltammetry and impedance measurements of the hOR1A1 receptor selectively immobilized on a gold electrode in the absence and presence of the agonists. Binding induces a decrease in the capacitive response of the receptor that is proportional to the ligand affinity, and which is attributed to changes in the magnitude and orientation of the electric dipole in the receptor, regulating its response to the applied electric field.

Keywords

Selectivity, olfactory receptor, agonist, impedance, specific capacitance, electric dipole.

Introduction

Olfactory receptors (ORs) are cell membrane proteins found primarily in olfactory sensory neurons (OSNs). Each OSN expresses a single type of OR, which once bound to an odorant ligand undergoes a conformational change that activates the cell signaling cascade and neuronal firing[1,2]. An OR has variable affinity for a subset of odorants and a single odorant can activate multiple receptors with different affinities[3]. The combinatorial effect of this variable regulation in the OSNs gives rise to the sense of olfaction. In vertebrates, ORs belong to the family of class A (rhodopsin-like) G protein-coupled receptors (GPCRs). They are expressed by about 400 genes in humans, accounting for half of the class A GPCRs, and consist of two major subfamilies, including the less abundant fish-like ORs (class I), which respond to water-soluble carboxylic acid-based odorants, and the mammalian-like receptors (class II), which respond to more hydrophobic compounds[4].

The expression of ORs, however, is not restricted to the olfactory system; they are also present in non-olfactory peripheral tissues such as the brain and the pancreas among others, where they are involved in different regulatory pathways and pathologies[5–7], thus emerging as candidate pharmacological targets. However, to date no clinical drug against ORs has been developed, mainly due to the lack of experimental structures. The structural basis of odorant recognition by vertebrate ORs remains elusive due to the difficulty of their heterologous expression and poor stability[8], and so far only the structure of human class I OR51E2 bound to the odorant propionate has been resolved[9].

The human olfactory system can discriminate between thousands of different volatile compounds, remarkably including those with very similar molecular structures[10,11]. The sensitivity and selectivity of odorant recognition by ORs has led to the development of biohybrid sensors for the detection of volatile organic compounds, reporting up to femtomolar concentration levels and good selectivity for specific odorants versus nonspecific odorants[12–17]. The highest levels of selectivity in terms of odorant discrimination have been described for electronic noses (e-noses) based on the immobilization of homochiral arrayed metal-organic structures or peptides that mimic the chiral nature of the OR-odorant interaction, and that allowed to distinguish between enantiomeric compounds[18,19].

However, the physiological discrimination of odorants ultimately relies on the selectivity of ORs, which is given by their tertiary structure. Here we disclose a method that allows odorant discrimination based on the modulation of the capacitive response of the OR. The results show the differentiation of three high affinity agonists based on their binding interaction to human OR1A1 (hOR1A1) selectively immobilized on a gold electrode and capacitance measurements.

Results

hOR1A1 was overexpressed in a stable, tetracycline inducible HEK293S GnTI$^-$ cell line as described[20]. The receptor was engineered by inserting the epitope tags FLAG at the N-terminal and rho1D4 at the C-terminal to allow its purification and detection. Here, the rho1D4 located at the C-terminus was used for the selective immobilization of the OR on the polished surface of the single-crystalline gold Au(111) electrode through anti-rhodopsin half antibody[21], thus providing a homogeneous orientation (Figure 1A). Electrode coverage was assessed by atomic force microscopy (AFM) (Figure 1B). Experiments were conducted in a custom-made electrochemical cell in a three-electrode configuration with a Pt/Ir wire as a counter electrode and Ag/AgCl (SSC) as reference (Figure 1C). All measurements were performed in 50 mM phosphate buffer pH = 7.4.

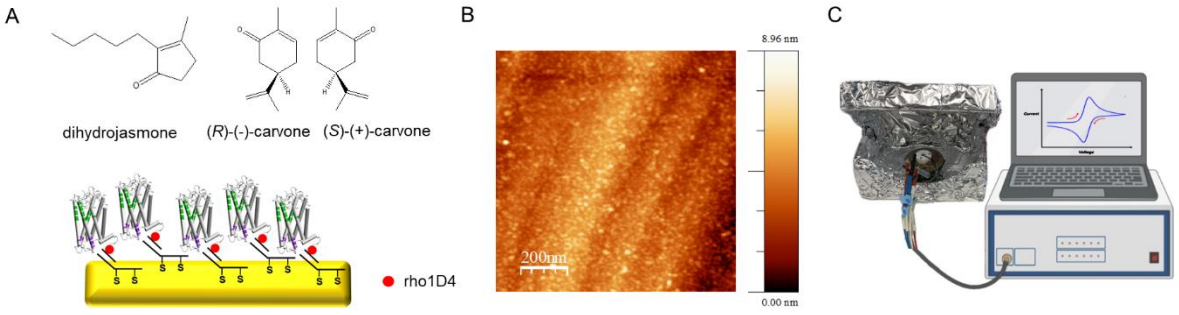

Figure 1. Experimental set-up. **A.** Molecular structures of the odorants used in this study, and scheme of the selective immobilization of hOR1A1 through rho1D4 C-terminal tag in the gold electrode. **B.** Representative AFM height image of the coverage of hOR1A1 immobilized by half anti-Rhodopsin on the gold electrode. **C.** Schematics of the electrochemical cell in the three-electrode configuration connected to the potentiostat.

Previous results of our group from electrochemical scanning tunneling microscopy (EC-STM) measurements, showed that binding of the cognate agonist dihydrojasmone to hOR1A1 caused a dose-dependent shift toward lower values of the open-circuit voltage in the receptor's I-V response. This was translated into a specific capacitance drop in cyclic voltammetry (CV) measurements[22]. Here, we conducted CV of hOR1A1 in response to binding of the two enantiomeric carvones, (*R*)-(-)-carvone and (*S*)-(+)-carvone. The two enantiomers are distinguishable by the human olfactory system as spearmint and caraway odors and bind to hOR1A1 showing lower affinities than dihydrojasmone (Supplementary Figure S1). For the measurements, the electrode potential was swept from 0.05 V to 0.30 V at different scan rates (Figure 2A). The specific capacitance (C_S) calculated from the voltammograms (Supplementary Tables 1 and 2), was normalized to the corresponding capacitance of the receptor alone, measured in the same experiment to avoid biasing from the variability of electrode coverage, and expressed as an increment. As observed for dihydrojasmone[22], binding of the carvone ligands to the receptor caused a decrease in C_S and the measured difference is reduced with the increasing scan rate (Figure 2B). The decrease in C_S produced by (*R*)-(-)-carvone and (*S*)-(+)-carvone is significantly lower than that produced by dihydrojasmone at 581 mV/s. Statistically significant differences were also found between the two carvone enantiomers (Figure 2C).

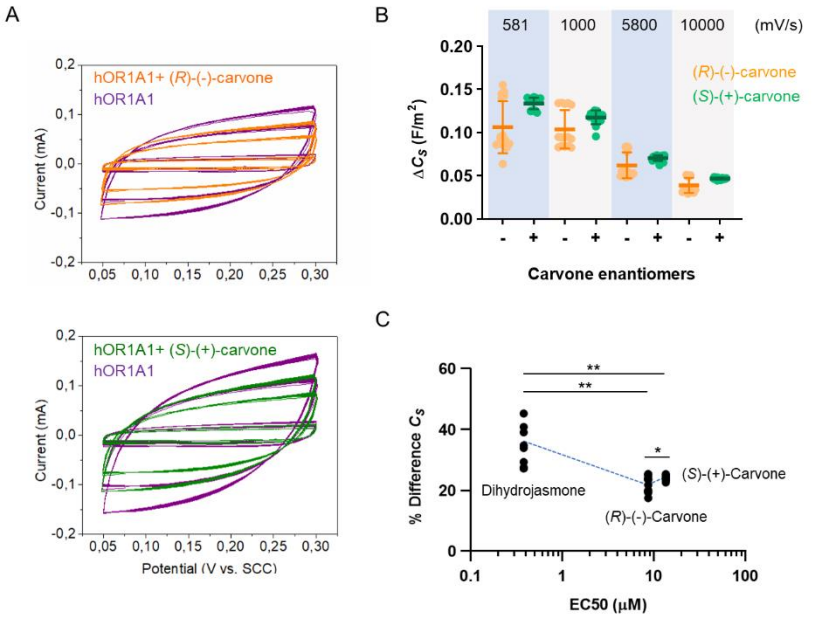

Figure 2. Specific capacitance (C_S) reduction by ligand binding. **A.** Representative cyclic voltammograms obtained for hOR1A1 before (purple) and after incubation with (*R*)-(-)-carvone (orange) or (*S*)-(-)-carvone (green), by sweeping the electrode potential from 0.05 to 0.30 V at increasing scan rates (581, 1000, 5800, and 1000 mV/s). **B.** Specific capacitance variation introduced by the ligand at the different scan rates calculated from the corresponding voltammograms. To avoid the bias from differences in electrode coverage across different experiments, the specific capacitance was expressed as an increment of the values measured in the same experiment: $\Delta C_S = C_S$ (hOR1A1)-C_S (ligand). (*R*)-(-)-carvone (orange) and (*S*)-(-)-carvone were noted as "-" and "+", respectively in the x-axis. n = 15, N = 3. **C.** Representation of the ΔC_S at its maximum (scan rate = 581 mV/s) versus ligand EC_{50}, showing ligands produce a significant decrease in capacitance. For dihydrojasmone: n = 10, N = 2 and for carvones n =15, N = 3. Significant differences

were judged through a Brown-Forsythe and Welch ANOVA tests (significantly different standard deviations). Family wise and confidence level of 0.05. **P<0.01, *P <0.05.

In Figure 2, the shape of the voltammograms is slightly sloped, revealing a non-ideal capacitive behavior. This is not considered to calculate the specific capacitance values from voltammetry, which depend on the scanning rate (Figure 1B). To account for this non-ideal response, we used potentiostatic electrochemical impedance spectroscopy (PEIS) in the 500 mHz-100 kHz range with an applied sinus amplitude of 10 mV, and zero polarization[23]. Complex-plane impedance plots (Nyquist plots) are shown in Figure 3A. The absence of a depressed semicircle evidences the non-Faradaic (capacitive) nature of the process. Also, a deviation from ideal behavior can be observed in the form of a tilted straight line in the impedance response[24]. The *x*-intercept at higher frequency, which is considered as the sum of the electrode resistance, the bulk electrolyte resistance, and the contact resistance between the electrode and the current collector[25], shows values between the 100-200 ohm (insets in Figure 3A). PEIS spectra were fitted using a constant phase element (CPE) (Supplementary Figure 2) and pseudocapacitance values were obtained from CPE parameters and Brug's equation, as previously described (see Supplementary Information and Supplementary Table S3)[23]. The C_S values from the PEIS fit are lower than those obtained by voltammetry. However, they reproduce a trend like that of the voltammetry results, showing a decrease in hOR1A1 capacitance according to binding affinity (Figure 3B). When an overpotential of +150 mV is applied, the C_S values increase by an order of magnitude (Supplementary Figure 3 and Table S4), and the differences introduced by the ligand also increase, yet the trend with ligand binding is maintained. Dispersion is reduced and some significant differences emerge (Figure 3C). We also examined the complex capacitance calculated from impedance measurements. The imaginary part of the complex capacitance (C'') is related to the irreversible energy dissipation and corresponds to the relaxation process. The relaxation time constant (τ) of the system can be determined from the peak frequency (relaxation frequency, f_R) in the C'' vs. frequency plots (Figure 3D) (see Supplementary Information).

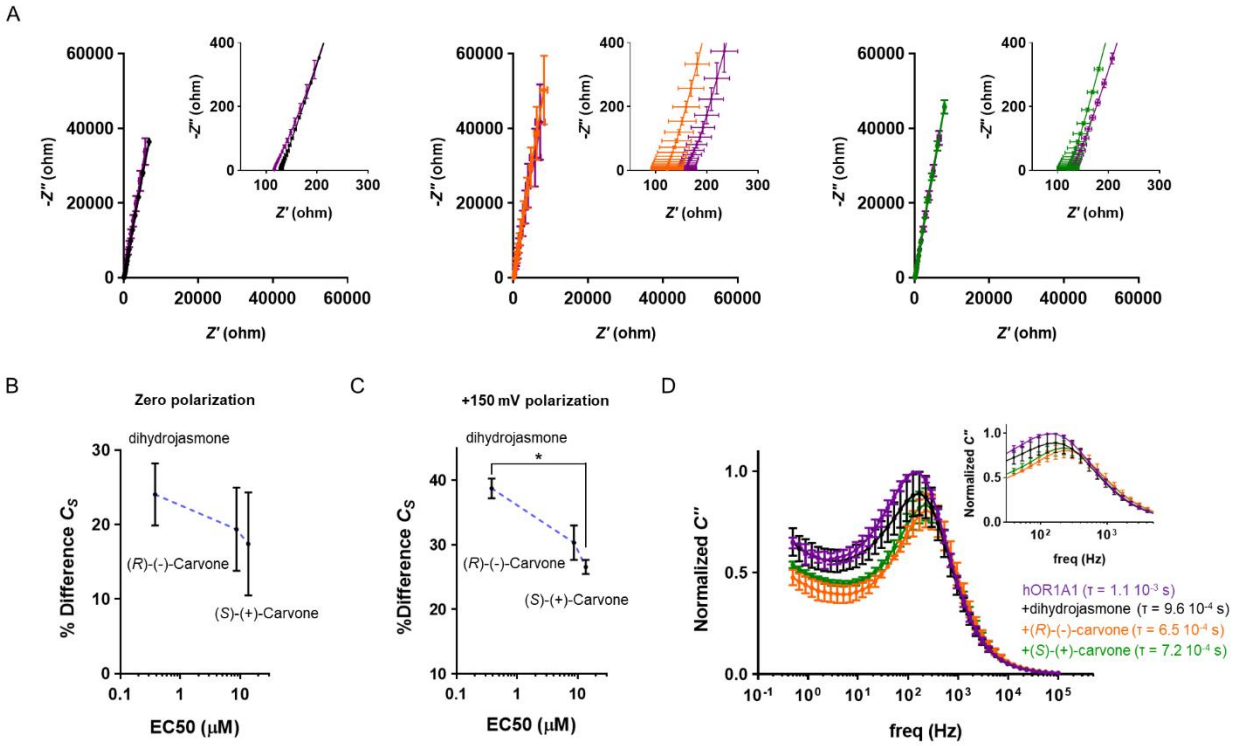

Figure 3. Potentiostatic electrochemical impedance spectroscopy (PEIS). **A.** Averaged Nyquist plots obtained for hOR1A1 before (purple) and after incubation with the corresponding ligand: dihydrojasmone (black), (*R*)-(-)-carvone (orange) or (*S*)-(-)-carvone (green). Insets show the *x*-intercept at high frequency between 100-200 ohm. n = 10 and N = 2 for dihydrojasmone and N = 3 for carvones. **B.** Representation of the ΔC_S versus ligand EC_{50} at zero polarization. C_S values were obtained by fitting the PEIS spectra using a CPE in series with a resistor, and Brug's equation (see Supplementary Information). n = 10 and N = 2 for dihydrojasmone and (*R*)-(-)-carvone, and N = 3 for (*S*)-(-)-carvone. **C.** Representation of the ΔC_S versus ligand EC_{50} at +150 mV polarization. C_S values were obtained by fitting the PEIS spectra using two CPE and a resistor in series[26], and Brug's equation (see Supplementary Information). n = 5 and N = 2. Significant differences were judged through a Brown-Forsythe and Welch ANOVA tests (significantly different standard deviations). Family wise and confidence level of 0.05. *P <0.05. **D.** Normalized C'' versus frequency plots obtained at zero polarization. Relaxation time constant (τ) of the system has been determined from the peak frequency. Inset shows a zoom-in of the peak. n = 10 and N = 2 for dihydrojasmone and N = 3 for carvones. Measurements were conducted in the 500 mHz-100 kHz range with an applied sinus amplitude of 10 mV.

At the molecular level, the results suggest that ligand binding limits the response of the receptor to an external electric field, most likely by altering its charge distribution as predicted by Reggiani and Alfinito[27,28]. Previous work has shown that low-order multipole moments can provide a good signature of the charge distribution of proteins[29]. Based on this and taking into account that upon ligand binding, the receptor undergoes a conformational change from the inactive to an active state[30], we calculated the magnitudes of the electrostatic dipole moment (μ) and its orientation in the predicted active and inactive alpha-fold structures for hOR1A1[31]. For these calculations, we used the actual sequence of the receptor from the experiments, which contains both the FLAG tag at the N-terminus and a Rho1D4 tag at the C-terminus. We produced up to 100 different models to explore the conformational landscape and charge distribution for both active and inactive states.[32–34] Proteins were aligned in the membrane normal plane[35] and dipole moments were calculated following equation (1):

$$\vec{\mu} = \sum_i q_i \vec{r}_i \qquad (1)$$

where q_i is the atomic charge and $\vec{r}_i$ its position vector.

The distributions of dipole moment magnitudes for the distinct activation states of hOR1A1 are presented in Figure 4. Results show that the conformational switch introduces changes in both the magnitudes and orientations of the electrostatic dipole. For the active state, we obtain a lower μ with a significant deviation from the *z*-axis (direction of the electric field in the experimental set-up), whereas the inactive state exhibits a higher μ, more aligned with the *z*-axis. Statistical analysis confirms that these distributions are significantly different, underscoring a distinct electrostatic rearrangement between the two states and anticipating a different response towards an applied electric field. In agreement with the experimental observations, when the receptor is in its active state, the lower dipole moment and its deviation from the z-axis might alter the receptor's overall response towards the electric field, potentially decreasing its sensitivity to it. Conversely, in the inactive state, the higher dipole moment aligned with the z-axis could enhance the receptor's alignment with the applied electric field, leading to an increased response.

To verify that the calculated shifts are inherent properties of the protein not influenced by the highly flexible regions, introduced by FLAG and Rho1D4 tags, we have these tags removed and electric dipole distributions recalculated (Supplementary Figure 4). This adjustment resulted in a narrower distribution due

to a smaller radius of gyration of the protein, yet the shifts remained similar, suggesting that this property is intrinsic to the protein.

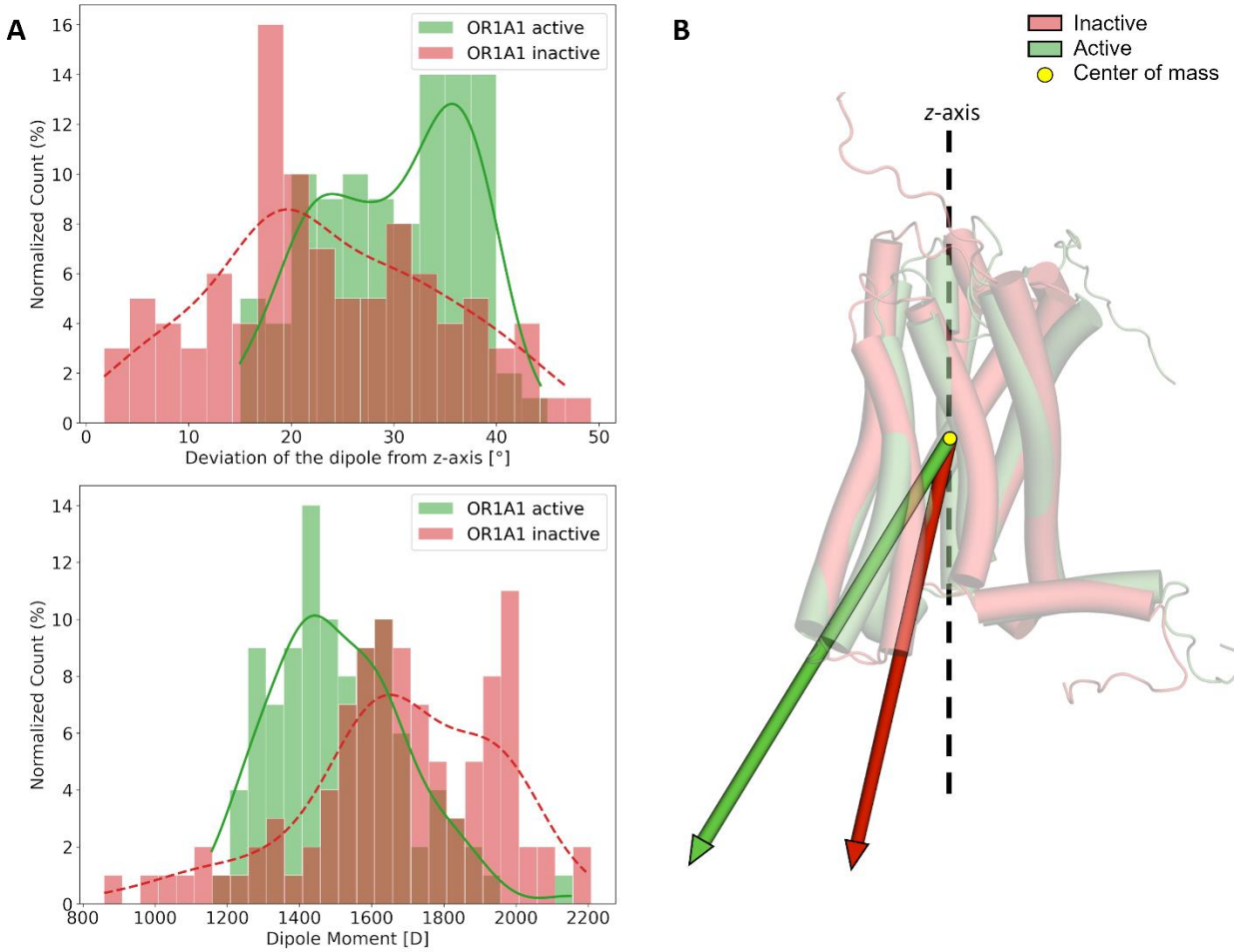

Figure 4. Shift in the electrostatic dipole of hOR1A1 along the conformational change. **A.** Normalized histograms showing the distribution of electric dipole magnitude and of the dipole moment vector deviation from the *z*-axis for 100 models in the active conformation (green, solid line smoothed distribution) and inactive conformation (red, dashed line smoothed distribution). **B.** 3D representation of the average structures: the active conformation of hOR1A1 is shown in green and the inactive conformation in red. Arrows represent the dipole moment vectors from the center of mass, deviating from the direction of the applied electric field (*z*-axis) for the active and inactive conformations. Statistic differences were judged by Mann-Whitney U test, with P-values of 0.5×10^{-9} and 2.6×10^{-6} for the magnitude of the dipole moment and the deviation from the *z*-axis, respectively.

The obtained distributions of the electrostatic dipole for the distinct activation states of hOR1A1 were compared with other class A GPCRs that have experimentally determined structures available in both active and inactive states (Supplementary Figure 5). Similar shifts in the magnitude of the dipole moment and its

deviation from the *z*-axis were obtained, indicating that our modeling accurately represents the active and inactive conformations of OR1A1. Interestingly, μ in the inactive state is lower for the studied GPCRs, in contrast to hOR1A1.

Discussion

Mechanisms of odor discrimination rely on the differential interactions of odorant molecules with ORs. Accordingly, several studies with OR-based biosensors demonstrated selectivity towards specific versus non-specific odorants[12–17]. The most recent studies on the deorphanization of ORs provide a classification of the set of ligands known to activate a receptor with different binding affinities, which is a crucial step in the study of olfactory perception, including receptor activity, as well as the impact of the molecular structure and physicochemical properties of odorant molecules on receptor selectivity[13].

We have recently reported the capacitive drop in hOR1A1 upon binding of the cognate ligand dihydrojasmone, quantifiable both at the single molecule level and in bulk experiments[22]. Here, starting from the same experimental setup, we studied the capacitive response of hOR1A1 in the presence of three high affinity agonists including dihydrojasmone and the two enantiomeric forms of carvone (*R*)-(-)-carvone over (*S*)-(+)-carvone, all distinguishable by the human olfactory system. The analysis of CV data allowed us to calculate the percentage of decrease in capacitance introduced by the ligand, which resulted significantly higher for dihydrojasmone compared to carvones. However, the non-ideal capacitive behavior noted as an apparent slope in the CV traces with respect to the *x*-axis resulted in the overestimation of the capacitance values obtained from voltammetry measurements, which also show dependence on the scanning rate[23]. Alternatively, we conducted impedance analysis using an equivalent circuit with a CPE. We demonstrate that ligand binding causes a decrease in receptor C_S depending on its binding affinity, allowing the differentiation between the three different high affinity agonists, and showing some selectivity for (*R*)-(-)-carvone over (*S*)-(+)-carvone, in agreement with activity measurements described for hOR1A1 in heterologous cell lines[36].

The increase in selectivity that allows us to see differences between agonists of the same receptor, with respect to previous measurements[16,17], could be attributed to different factors including the configuration of the measurement setup, and the capacitive-based response that is directly linked to an intrinsic property of the receptor (the electric dipole), as demonstrated by theoretical calculations. Here the receptor was immobilized using a monoclonal half antibody against the C-terminal rho1D4 tag, resulting in a setting in which the receptor is homogeneously oriented and closer to the electrode than in conventional self-assembled multilayer systems[37,38], thus reducing interfacial contributions and improving the electrical contact. The decrease in specific capacitance is interpreted as an alteration in the charge distribution of the receptor[27,28], which limits its polarization in response to an external electric field. The results of the calculations, which include 100 different models of the alpha-fold structures predicted for active and inactive conformations of hOR1A1, show that for the active form of the receptor a significantly smaller dipole moment is obtained that is less aligned with the direction of the applied field, potentially decreasing its sensitivity to it. This could also explain the significance observed in voltammetry, where the applied field is stronger (ΔV = 250 mV) compared to EIS measurements (ΔV = 10 mV sine wave amplitude). This is also seen when applying an overpotential to the electrode in PEIS measurements, where probably the initial prepolarization of the charges in the receptor makes the differences introduced by the ligand more evident.

Modeling of the electric dipole distribution for other class A GPCRs leads to shifts like those obtained for hOR1A1 in both the magnitude and orientation of the dipole, suggesting that the observed shifts may be a conserved feature in class A GPCRs. However, unlike in hOR1A1, the magnitude of the dipole moment in

the inactive state is smaller for the two class A GPCRs studied. This difference may be attributed to slight variations in the conformational change of TM6 in ORs, where the intracellular part moves outward while the extracellular part moves inward[39,40]. Such binding-based discrimination poses the possibility of capacitance measurements to reach efficacy-driven odorant selectivity towards target receptors without stimulating off-target receptors, a feature of great interest to the pharmaceutical industry particularly for GPCRs[41].

Limitations of the study regarding practical application include the poor stability and production cost of full protein ORs, which could ultimately be replaced by peptide-based mimetics that effectively reproduce the receptor binding regions[12]. This alternative could benefit from recent improvements in molecular modeling, site-directed mutagenesis and functional expression studies, and from future experimentally determined structures available. Also, the study considers only high affinity ligands of hOR1A1, so further exploration of sensitivity and selectivity in the capacitive response to other lower affinity ligands is required, as well as in other ORs. This will require optimization of the experiment to enable high-throughput screening.

In conclusion, we unveil a method to detect odorants based on their binding interaction with the olfactory receptor, thus mimicking physiological odor decoding. Ligand binding induces a decrease in the capacitive response of the receptor that is proportional to the ligand affinity, and which is attributed to changes in the magnitude and orientation of the electric dipole in the receptor, thereby modulating its sensitivity to an external electric field.

Materials and Methods

Materials

Anti- Rhodopsin (CT, last 9 amino acids, clone Rho 1D4, Chemicon®) monoclonal antibody 1 mg/mL produced in mouse, Whatman® Anotop® 25 Plus syringe filters (pore size 0.02 µm, glass microfiber prefilter, sterile), sodium phosphate monobasic monohydrate (BioXtra, for molecular biology, ≥ 99.5%), sodium phosphate dibasic dihydrate (BioUltra, for molecular biology, ≥ 99.0%), deionized water (18 MΩ cm^{-1} < 4 ppb TOC, Milli-Q) and dihydrojasmone (≥ 98%, stabilized, FG), (-)-carvone (≥ 99.0%, analytical standard), (+)-carvone (≥ 98.5%, analytical standard), sulfuric acid 95-98% and 33% *w/v* hydrogen peroxide were purchased from Merck (Madrid, Spain). Bond-Breaker™ TCEP 0.5 M solution, Neutral pH, was from Thermo Scientific™ (Thermo Fisher Scientific, Barcelona, Spain). Atomically flat Au(111) single-crystal disks (dia. 10.00 mm x thickness/length 1.00 mm as cut, one side polishing with roughness < 0.01 micron and orientation accuracy < 0.1 deg.) were from MaTecK GmbH (MaTeck Material Technologie & Kristalle GmbH, Jülich, Germany). Silicon AFM probes were purchased from Budget Sensors (NanoAndMore GmbH, Germany). Pt80/Ir20 wire (0.25 mm, temper hard) was purchased from Advent (Advent Research Materials Ltd, Witney, UK). Miniaturized ultralow leakage membrane Ag/AgCl (SSC) reference electrode filled with 3M KCl (DRIREF-2SH) was from World Precision Instruments (World Precision Instruments-EU, Hertfordshire, UK).

Sample preparation

hOR1A1 was expressed in a stable tetracycline-inducible HEK293S cell line and engineered by inserting a C-terminal rho1D4 epitope tag and an N-terminal FLAG epitope tag to allow its purification and detection, as previously described[20]. TCEP solutions for Anti-Rhodopsin reduction were prepared in 10 mM phosphate buffer (pH = 7.4) at 5 mM. A volume of 10 µL of TCEP was added to 1 mL of 10 µg/mL Anti- Rhodopsin

in 10 mM phosphate buffer (pH = 7.4) and allowed to react at room temperature for 60 min (incubation solution). Atomically flat Au(111) single-crystal were flame annealed and electrochemically polished prior to use. Au(111) electrode was incubated with 150 µL of the incubation solution for 24 h at 4ºC. Afterwards, the incubation solution was removed, the electrode was washed with 10 mM phosphate buffer (pH = 7.4) and dried. Then, it was incubated with 150 µL of fresh monomeric hOR1A1 in PBS-0.2% FC14 buffer[20], at room temperature for 60 min. After this time, the Au(111) electrode was washed with copious amounts of the measuring buffer (50 mM phosphate buffer pH = 7.4), connected to the electrochemical cell, and the cell filled with 250 µL of the measuring buffer.

Prior to any functionalization, the electrochemical cell was cleaned with piranha solution (3:1 v/v solution of H_2SO_4 and H_2O_2). *Caution: piranha solution is a strong oxidizer and a strong acid. It should be handled with extreme care, as it reacts violently with most organic materials.*

For ligand binding experiments, the cell was disconnected, the buffer removed, and the cell filled with 250 µL of the ligand solution at saturation concentration (30 µM for dihydrojasmone and 2 mM for carvones)[20,42], in the measuring buffer. After 1h of incubation at room temperature, the solution was removed, and the cell filled again with the measuring buffer.

Atomic force microscopy (AFM)

Surface coverage was investigated by AFM measurements as previously described[22]. Briefly, Au(111) samples with hOR1A1 immobilized by half anti-Rhodopsin were imaged with tapping mode in air using silicon AFM probes with a spring constant k = 40 N/m and a resonant frequency v = 300 kHz. At least, four images of 1μm^2 were taken per sample.

Electrochemical measurements

Measurements were carried out using a potentiostat SP-150 controlled EC-Lab® software (Bio-Logic, Spain) at room temperature (23 ± 2 ºC). Deionized water was used to prepare all solutions and for rinsing samples and electrodes. All solutions were degassed with nitrogen. A homemade electrochemical liquid cell with a standard sample plate was used in four-electrode configuration, using a 0.25 mm diameter Pt80/Ir20 wire as a counter electrode, a miniaturized ultralow leakage membrane Ag/AgCl (SSC) reference electrode filled with 3M KCl and a Au(111)-based working electrode (WE). All electrochemical measurements

were performed in a Faraday cage. Cyclic voltammograms were recorded from 0.050 V to 0.300 V at the different scan rates ($E_i = E_f = 0.250V$)[22]. At least 50 cyclic voltammograms were registered at each scan rate. Specific capacitance (C_s) was obtained as previously reported[22,43], using the following equation:

$$C_S = \frac{dQ}{dV} = \frac{1}{Av\Delta V}\int_{V_1}^{V_2} I(V)dV$$

Where $\int_{V_1}^{V_2} I(V)dV$ is the hysteresis loop area, ΔV is the range of potential, v is scan rate, and A is the area of the electrode.

Potentiostatic electrochemical impedance spectroscopy (PEIS) measurements were conducted in the 500 mHz-100 kHz frequency range with an applied sinus amplitude of 10 mV, and zero polarization. At least 10 repeats were taken for each measure. Experimental EIS data were fitted by the ZView 4 software. All electrode potentials are reported vs SSC.

Electric dipole calculations

For hOR1A1 Multistate AlphaFold2 procedure was used[31], generating one active and inactive conformation. From those two starting conformations, Modeller (v10.5)[34] was used to generate 100 new structures to sample the conformational space. VTFM optimization with 300 iterations maximum was used as well as slow MD refinement. Other parameters were kept at their default values.

Prior to calculating the dipole moment of the studied protein, their protonation states were determined using Propka[33]. Next, the all-atoms force field FF14SB[32] from Amber20 was used to assign atomic charges. Then, proteins were aligned along the z-axis using the OPM webserver[35]. Dipole moments were calculated using equation (1).

Acknowledgements

This work was supported by the Biomedical Research Networking Center (CIBER), Spain. CIBER is an initiative funded by the VI National R&D&i Plan 2008–2011, Iniciativa Ingenio 2010, Consolider Program, CIBER Actions, and the Instituto de Salud Carlos III, with the support of the European Regional Development Fund (ERDF). This work was funded by the CERCA Program and by the Commission for Universities and Research of the Department of Innovation, Universities, and Enterprise of the Generalitat de Catalunya (2021 SGR 01545, 2021 SGR 01410). This work was also partly supported by grants from the Conseil Régional Bourgogne, Franche-Comte (PARI grant), the FEDER (European Funding for Regional Economic Development), and by the Agence Nationale de la Recherche (ANR). M.L. was supported by the Fondation Roudnitska under the aegis of Fondation de France and by GIRACT (Geneva, Switzerland).

References:

1. Francia, S. & Lodovichi, C. The role of the odorant receptors in the formation of the sensory map. *BMC Biology 2021 19:1* **19**, 1–18 (2021).

2. Boccaccio, A. Patch-clamp recordings from mouse olfactory sensory neurons. *Methods in Molecular Biology* **1820**, 113–122 (2018).

3. Saito, H., Chi, Q., Zhuang, H., Matsunami, H. & Mainland, J. D. Odor coding by a mammalian receptor repertoire. *Sci Signal* **2**, (2009).

4. Buck, L. & Axel, R. A novel multigene family may encode odorant receptors: a molecular basis for odor recognition. *Cell* **65**, 175–187 (1991).

5. Li, M. *et al*. Olfactory receptor 5B21 drives breast cancer metastasis. *iScience* **24**, 103519 (2021).

6. Yang, Z., Cheng, J., Shang, P., Sun, J. P. & Yu, X. Emerging roles of olfactory receptors in glucose metabolism. *Trends Cell Biol* **33**, 463–476 (2023).

7. Herrmann, T., Koeppel, C., Linn, J., Croy, I. & Hummel, T. Olfactory brain activations in patients with major depressive disorder. *Sci Rep* **13,** 10072 (2023).

8. Designed Research; K, H. M. I., Performed Research; K, M. Y. I. & Pnas, M. Structural instability and divergence from conserved residues underlie intracellular retention of mammalian odorant receptors. *Biol Sci* **117**, 2957-2967 (2020).

9. Billesbølle, C. B. *et al*. Structural basis of odorant recognition by a human odorant receptor. *Nature* **615**, 742–749 (2023).

10. Brenna, E., Fuganti, C. & Serra, S. Enantioselective perception of chiral odorants. *Tetrahedron: Asymmetry* **14**, 1–42 (2003).

11. Feng, G. & Zhou, W. Nostril-specific and structure-based olfactory learning of chiral discrimination in human adults. *Elife* **8**, e41296 (2019).

12. Wasilewski, T. *et al*. Olfactory receptor-based biosensors as potential future tools in medical diagnosis. *TrAC, Trends Anal Chem* **150,** 116599 (2022).

13. Barbosa, A. J. M., Oliveira, A. R. & Roque, A. C. A. Protein-and peptide-based biosensors in artificial olfaction. *Trends Biotechnol* **36**, 1244–1258 (2018).

14. Yoon, W. *et al*. Polypyrrole nanotubes conjugated with human olfactory receptors: High-Performance transducers for FET-Type bioelectronic noses. *Angew Chem Int Ed* **48**, 2755–2758 (2009).

15. Park, S. J. *et al*. Ultrasensitive flexible graphene-based field-effect transistor (FET)-type bioelectronic nose. *Nano Lett* **12**, 5082–5090 (2012).

16. Lee, S. H. *et al*. Mimicking the human smell sensing mechanism with an artificial nose platform. *Biomaterials* **33**, 1722–1729 (2012).

17. Goldsmith, B. R. *et al*. Biomimetic chemical sensors using nanoelectronic readout of olfactory receptor proteins. *ACS Nano* **5**, 5408–5416 (2011).

18. Maho, P. *et al*. Reliable chiral recognition with an optoelectronic nose. *Biosens Bioelectron* **159**, 112183 (2020).

19. Okur, S. *et al*. An Enantioselective e-Nose: An Array of Nanoporous Homochiral MOF Films for Stereospecific Sensing of Chiral Odors. *Angew Chem Int Ed* **60**, 3566–3571 (2021).

20. Belloir, C., Miller-Leseigneur, M. L., Neiers, F., Briand, L. & Le Bon, A. M. Biophysical and functional characterization of the human olfactory receptor OR1A1 expressed in a mammalian inducible cell line. *Protein Expr Purif* **129**, 31–43 (2017).

21. Sharma, H. & Mutharasan, R. Half antibody fragments improve biosensor sensitivity without loss of selectivity. *Anal Chem* **85,** 2472-2477 (2013).

22. Lagunas, A., Belloir, C., Briand, L., Gorostiza, P. & Samitier, J. Determination of the nanoscale electrical properties of olfactory receptor hOR1A1 and their dependence on ligand binding: Towards the development of capacitance-operated odorant biosensors. *Biosens Bioelectron* **218**, 114755 (2022).

23. Gateman, S. M. *et al*. On the use of a constant phase element (CPE) in electrochemistry. *Curr Opin Electrochem* **36**, 101133 (2022).

24. Mulder, W. H. & Sluyters, J. H. An explanation of depressed semi-circular arcs in impedance plots for irreversible electrode reactions. *Electrochim Acta* **33**, 303–310 (1988).

25. Mei, B. A. *et al*. Physical Interpretations of Electrochemical Impedance Spectroscopy of Redox Active Electrodes for Electrical Energy Storage. *J Phys Chem C* **122**, 24499–24511 (2018).

26. Euch, S. EL *et al*. Temperature dependence of the electrochemical behavior of the 690 Ni-base alloy between 25 and 325 °C. *Electrochim Acta* **317**, 509–520 (2019).

27. Reggiani, L., Millithaler, J. F. & Pennetta, C. Microscopic modeling of charge transport in sensing proteins. *Nanoscale Res Lett* **7**, 1–7 (2012).

28. Alfinito, E. & Reggiani, L. Current-voltage characteristics of seven-helix proteins from a cubic array of amino acids. *Phys Rev E* **93,** 062401 (2016).

29. Lošdorfer Božič, A. & Podgornik, R. pH Dependence of charge multipole moments in proteins. *Biophys J* **113**, 1454–1465 (2017).

30. De March, C. A. *et al*. Conserved residues control activation of mammalian G protein-coupled odorant receptors. *J Am Chem Soc* **137**, 8611–8616 (2015).

31. Jumper, J. *et al*. Highly accurate protein structure prediction with AlphaFold. *Nature* **596**, 583–589 (2021).

32. Maier, J. A. *et al*. ff14SB: Improving the accuracy of protein side chain and backbone parameters from ff99SB. *J Chem Theory Comput* **11**, 3696–3713 (2015).

33. Søndergaard, C. R., Olsson, M. H. M., Rostkowski, M. & Jensen, J. H. Improved treatment of ligands and coupling effects in empirical calculation and rationalization of pKa values. *J Chem Theory Comput* **7**, 2284–2295 (2011).

34. Webb, B. & Sali, A. Comparative protein structure modeling using MODELLER. *Curr Protoc Bioinformatics* **54**, 5.6.1-5.6.37 (2016).

35. Lomize, M. A., Pogozheva, I. D., Joo, H., Mosberg, H. I. & Lomize, A. L. OPM database and PPM web server: resources for positioning of proteins in membranes. *Nucleic Acids Res* **40**, D370 (2012).

36. Flavour science: Proceedings from XIII Weurman Flavour Research Symposium - Google Books. https://books.google.es/books?hl=en&lr=&id=eUITAAAAQBAJ&oi=fnd&pg=PP1&ots=tfD_8-RDqu&sig=A-eE7FNF4ZOwFWw727_AZp-UEr4&redir_esc=y#v=onepage&q&f=false.

37. Alfinito, E., Pennetta, C. & Reggiani, L. Olfactory receptor-based smell nanobiosensors: An overview of theoretical and experimental results. *Sens Actuators B Chem* **146**, 554–558 (2010).

38. Hou, Y. *et al*. A novel detection strategy for odorant molecules based on controlled bioengineering of rat olfactory receptor I7. *Biosens Bioelectron* **22**, 1550–1555 (2007).

39. Choi, C. *et al*. Understanding the molecular mechanisms of odorant binding and activation of the human OR52 family. *Nat Commun* **14**, 1–14 (2023).

40. Billesbølle, C. B. *et al*. Structural basis of odorant recognition by a human odorant receptor. *Nature* **615**, 742–749 (2023).

41. Powers, A. S. *et al*. Structural basis of efficacy-driven ligand selectivity at GPCRs. *Nat Chem Biol* **19**, 805–814 (2023).

42. Ben Khemis, I., Bouzid, M., Mechi, N. & Ben Lamine, A. Statistical physics modeling and interpretation of the adsorption of enantiomeric terpenes onto the human olfactory receptor OR1A1. *Int J Biol Macromol* **171,** 428-434 (2021).

43. Wang, C.-M. *et al*. The influence of specific surface area on the capacitance of the carbon electrodes supercapacitor. *The 3rd International Conference on Industrial Application Engineering 2015 (ICIAE2015)* (2015) doi:10.12792/iciae2015.077.